Article

Comparison of the Morrison and WDM6 Microphysics Schemes in the WRF Model for a Convective Precipitation Event in Guangdong, China, through the Analysis of Polarimetric Radar Data

Xiaolong Chen [1,2] and Xiaoli Liu [1,2,*]

1   China Meteorological Administration Aerosol-Cloud and Precipitation Key Laboratory, Nanjing University of Information Science and Technology, Nanjing 210044, China; 202212030021@nuist.edu.cn
2   College of Atmospheric Physics, Nanjing University of Information Science and Technology, Nanjing 210044, China
*   Correspondence: liuxiaoli2004y@nuist.edu.cn

Abstract: Numerical weather prediction (NWP) models are indispensable for studying severe convective weather events. Research demonstrates that the outcomes of convective precipitation simulations are profoundly influenced by the choice between single or double-moment schemes for ice precipitation particles and the categorization of rimed ice. The advancement of dual-polarization radar has enriched the comparative validation of these simulations. This study simulated a convective event in Guangdong, China, from May 7 to 8, 2017, employing two bulk microphysical schemes (Morrison and WDM6) in the WRF v4.2 model. Each scheme was divided into two versions: one representing rimed ice particles as graupel (Mor_G, WDM6_G) and the other as hail (Mor_H, WDM6_H). The simulation results indicated negligible differences between the rimed ice set as graupel or hail particles, for both schemes. However, the Morrison schemes (Mor_G, Mor_H) depicted a more accurate raindrop size distribution below the 0 °C height level. A further analysis suggested that disparities between the Morrison and WDM6 schemes could be attributed to the intercept parameter (N_0) setting for snow and graupel/hail in WDM6 scheme. The prescribed snow and graupel/hail N_0 of WDM6 scheme might influence the melting processes, leading to a higher number concentration but a reduced mass-weighted diameter of raindrops. Reducing the intercept parameter for snow and graupel/hail in the WDM6 scheme could potentially enhance the simulation of convective precipitation. Conversely, the increase in N_0 might deteriorate the precipitation simulation performance of the WDM6_G scheme, whereas the WDM6_H scheme exhibits minimal sensitivity to such changes.

Keywords: s-band polarimetric radar; convective precipitation; cloud microphysics

1. Introduction

Severe convective weather, including hail, tornadoes, and heavy rainfall, results from deep convection and is highly destructive, causing significant damage to industrial and agricultural sectors [1]. Accurate forecasting of such weather is crucial for disaster prevention and mitigation [2]. Numerical weather prediction (NWP) models, which are used to predict severe convective weather, depend heavily on cloud microphysics parameterization [3]. However, the limitations in understanding and parameterizing cloud microphysics introduce significant uncertainties into NWP forecasts [4–6].

In NWP models, microphysics schemes are categorized into bulk and bin schemes. Bulk schemes use semi-empirical descriptions of particle size distributions (PSDs) to characterize hydrometeor properties in clouds. Due to their computational efficiency, bulk schemes are commonly used for precipitation prediction and simulation [7]. Bulk schemes are classified as single-moment, double-moment, or triple-moment [8]. While triple-moment schemes offer more detail, they also incur higher computational costs [9]. Therefore, current NWP research mainly focuses on single-moment and double-moment schemes

due to their balance between accuracy and computational efficiency. Single-moment schemes predict one prognostic, the mass mixing ratio, whereas double-moment schemes predict both the mass mixing ratio and number concentration [10,11].

Studies have shown that convective precipitation simulations are sensitive to the choice between single-moment and double-moment schemes. By improving evaporation processes and size sorting, Morrison et al. and Dawson et al. found that double-moment schemes produce more accurate drop size distributions (DSDs) in idealized convective cases simulations [12,13]. Furthermore, when simulating real cases, Jung et al. found that compared to the Lin single-moment scheme, the Milbrandt and Yau (M-Y) double-moment scheme generated radar reflectivity more consistent with observations due to improved raindrop size sorting [14]. Similarly, Putnam et al. noted that the double-moment scheme more effectively simulated the cold pool, convective line, and stratiform region in mesoscale convective system (MCS) simulations, resulting in more accurate precipitation predictions [15].

In bulk microphysical schemes, hydrometeors are classified into liquid-phase and ice-phase particles. Ice particles, with their varied densities and complex shapes, significantly influence cloud microphysical processes and introduce uncertainty into convective precipitation simulations [8]. As computational power has advanced, the treatment of ice-phase processes in NWP has been improved. Rutledge and Hobbs initially included ice-phase processes in cloud microphysics, categorizing frozen hydrometeors as "cloud ice" and "snow" [16]. They later expanded the scheme to include rimed ice category, such as "graupel" or "hail", which is found to have a substantial impact on precipitation [17]. Research showed that adding rimed ice category strengthens simulated precipitation and aligns results more closely with observations [12,18]. Thereafter, bulk schemes, like Morrison and WDM6, allow rimed ice to represent either high-density, fast-falling hail or low-density, slower-falling graupel [12,19].

Numerical simulations of idealized supercell cases have shown that precipitation and convective cloud structure are sensitive to the rimed ice category [20,21]. Simulating the idealized case by Morrison scheme with graupel resulted in an unrealistically wide convective region compared to the scheme with hail [22]. Meanwhile, the WDM6 scheme with hail caused hail particles to fall out of the updraft quickly, minimizing melting or evaporation in the idealized simulation [23]. However, some studies suggested that the sensitivity of the rimed ice category to precipitation in real-case simulations is limited and might be influenced by specific environmental conditions [24,25]. Weverberg et al. extended the research to larger-scale, longer-duration simulations, finding that sensitivity may be less significant in idealized squall line simulations [26]. Therefore, it is crucial to explore the impact of rimed ice categories on precipitation over longer simulation durations in real convective processes.

Evaluating the effects of microphysical structures and convective cloud characteristics in simulations is challenging when only comparing precipitation and radar reflectivity with observations. Li et al. showed that while the NSSL scheme effectively simulated rainfall regions, it failed to accurately reproduce drop size distribution (DSD) [7]. Accurate observations of convective clouds are essential for evaluating simulations and understanding convective processes. The aircraft observations are limited and costly due to the unique flow field structures [27], while remote sensing provides higher temporal and spatial resolution. Traditional single-polarization Doppler radar provides limited microphysical information [6]. In contrast, dual-polarization radar transmits and receives polarized electromagnetic waves in two orthogonal directions, providing rich information about microphysical data on hydrometeors [28]. The polarimetric radar data (PRD) simulator converts numerical simulation variables into radar polarimetric quantities, facilitating direct comparison between simulation results and dual-polarization radar signals [29].

In recent years, PRD simulators have been widely used to evaluate microphysical schemes. Jung et al. and Snyder et al. simulated idealized supercell events to evaluate how well different schemes reproduce the characteristics of polarimetric radar observations [14, 30]. Zhou et al. used PRD simulator developed by Jung et al. to reexamine the effects of rain

breakup and evaporation efficiency on precipitation [14,31,32]. Köcher et al. employed the CR-SIM PRD simulator to analyze polarization variables for different schemes near Munich, Germany [3]. These studies demonstrate that PRD simulators provide detailed insights for evaluating numerical simulations of real convective precipitation. However, there is a need for further exploration of the effects of different microphysical parameterization settings, such as the choice of single or double moment, and rimed ice category in real convective precipitation simulations.

Although previous work has shown that precipitation simulation results are sensitive to the choice of single-moment or double-moment schemes for ice phase hydrometeors and rimed ice categories, the underlying microphysical processes remain unclear. Moreover, simulating severe convective weather in southeastern China, particularly Guangdong, poses challenges due to weak synoptic forcing and a moist environment [31]. To address this, we simulated a convective precipitation event in southeastern China using two bulk schemes: a fully double-moment scheme (Morrison) and a double-moment scheme for liquid-phase processes only (WDM6). Additionally, we compare the results of the two schemes with graupel and hail representing the rimed ice category, focusing on the sensitivity of convective precipitation to the properties of rimed ice particles. This research provides valuable insights into setting of microphysical schemes for summer convective precipitation simulations in southeastern China.

The article is organized as follows: Section 2 describes the data and methods used. Section 3 presents the evaluation and analysis of the results. Discussion and conclusions are provided in Section 4.

2. Materials and Methods

2.1. Model Configurations and Description of Physical Schemes

In this study, we use the Weather Research and Forecasting model (WRF v4.2) to simulate a mesoscale convective precipitation event in southern China from 18:00 UTC on 7 May to 18:00 UTC on 8 May 2017. The analysis focuses on the period from 00:00 UTC to 18:00 UTC on May 8, excluding a 6-h spin-up period. The simulation employs a two-way nested grid with 3 km and 1 km resolutions, with the innermost grid consisting of 481×481 grid points. The simulation domain is shown in Figure 1.
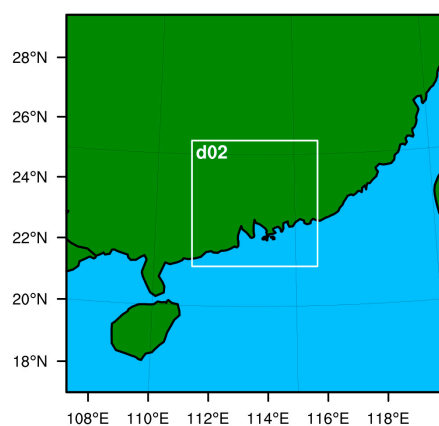

Figure 1. Nested domains of the WRF model simulation.

The initial and boundary conditions are derived from the fifth-generation European Centre for Medium-Range Weather Forecasts reanalysis data (ERA5). The planetary boundary layer scheme used is the Mellor-Yamada-Janjic (MYJ) scheme, and the surface layer scheme is the Eta Similarity scheme. The land surface scheme is represented by the unified Noah land-surface model. The Rapid Radiative Transfer Model (RRTM) for the Global Climate Model (GCM) scheme is for both shortwave and longwave radiation. Four different microphysical schemes setting are selected for the study: the Morrison scheme with graupel (Mor_G) and hail (Mor_H) representing rimed ice particles, and the WDM6

scheme with graupel (WDM6_G) and hail (WDM6_H) representing rimed ice-phase particles (Appendix A summarizes the main characteristics of Morrison and WDM6 schemes). In the Morrison scheme, graupel is assigned a density of 500 kg/m^3, while hail has a density of 900 kg/m^3. For the WDM6 scheme, graupel has a density of 500 kg/m^3 with an N$_0$ of 4×10^6 m^{-4}, and hail has a density of 700 kg/m^3 with an N$_0$ of 4×10^4 m^{-4}. The rimed ice category can be switched between graupel and hail based on these parameters. The microphysical variables predicted by the different schemes are presented in Table 1.

Table 1. Summary of microphysics options for WDM6 and Morrison scheme.

Scheme	Mixing Ratio	Number Concentration
WDM6	Q$_c$ Q$_r$ Q$_i$ Q$_s$ Q$_{g/h}$	N$_n$** N$_c$ N$_r$
Morrison	Q$_c$ Q$_r$ Q$_i$ Q$_s$ Q$_{g/h}$	N$_r$ N$_i$ N$_s$ N$_{g/h}$

N$_n$**: CCN number concentration, c: cloud, r: rain, i: ice, s: snow, g: graupel, h: hail.

2.2. Dual-Polarization Radar and Precipitation Data

Radar observation data were from the Guangzhou S-band polarimetric radar (GZPR). The GZPR is a dual-polarization radar with a wavelength of 10 cm, a beamwidth of 0.92°, a resolution of 0.25 km, and the sampling interval was set to be approximately 6 min. Polarimetric radar observations are susceptible to noise, necessitating the application of quality control to the radar data in this study. A threshold check was performed using a combination of the cross-correlation coefficient (ρ_{HV}), signal-to-noise ratio (SNR), and K$_{DP}$. The details can be found in [33]. After quality control, the polarimetric radar data were interpolated onto a Cartesian coordinate system with a horizontal grid spacing of 1 km and a vertical grid spacing of 200 m using the 88D2ARPS software in the Advanced Regional Prediction (ARPS) version 5.2.14 from the Center for Analysis and Prediction of Storms (CAPS). In polarimetric radar data, measurements of the radar reflectivity at horizontal polarization (Z$_H$), the differential reflectivity (Z$_{DR}$), the specific differential phase (K$_{DP}$), and ρ_{HV} are used to characterize precipitation processes. Beyond Z$_H$, the Z$_{DR}$, indicative of hydrometeor shape, and the K$_{DP}$ which primarily represents the liquid water content in a sample volume, are two frequently used polarimetric variables [28]. The precipitation data originate from a 0.1° grid dataset that merges hourly precipitation measurements from Chinese automatic surface stations with CMORPH retrievals [34]. This combined dataset includes both surface and satellite observations.

2.3. PRD Simulator Introduction

The PRD simulator developed by Center for Analysis and Prediction of Storms (CAPS) to simulate polarimetric variables using the WRF outputs [14,32,35]. This simulator employs the T-matrix method to create scattering amplitude lookup tables for all hydrometeor categories as a function of particle diameter, assuming a proportion of liquid water in ice categories. The hydrometeor PSD moments extracted from the WRF outputs are employed to calculate the intercept, shape, and slope parameters of the presupposed gamma distribution. The PRD simulator supports X, C, and S band wavelengths and is compatible with various microphysical schemes, including Lin, WSM6, Thompson, M-Y, Morrison, WDM6, and NSSL [35]. For this study, we only focused on the S-band wavelength for comparison with the radar observation data form the GZPR.

3. Results

3.1. The Evaluation of the Simulated Accumulation Rainfall

We compare accumulated precipitation from different schemes with observational data from Chinese automatic surface stations with CMORPH retrievals by Figure 2. This Figure shows the spatial distribution of 18-h surface accumulated precipitation from 00:00 to 18:00 on 8 May. According to the grade of precipitation (GB/T 28592-2012) [36], severe rainfall (12-h totals exceeding 30 mm) was mainly observed in central Guangdong Province. Other regions

experienced moderate to heavy rainfall (12-h totals between 5 and 30 mm). All four schemes underestimated precipitation intensity, predicting fewer areas of severe rainfall and generally simulating light to moderate precipitation (12-h totals between 1 and 15 mm) elsewhere. The Mor_G and Mor_H schemes, however, predicted larger and more concentrated areas of severe rainfall compared to the WDM6_G and WDM6_H schemes, though these areas still fell short of observed values. Additionally, the Mor_G and Mor_H schemes simulated more extreme heavy rainfall areas (12-h totals exceeding 70 mm) than observed.
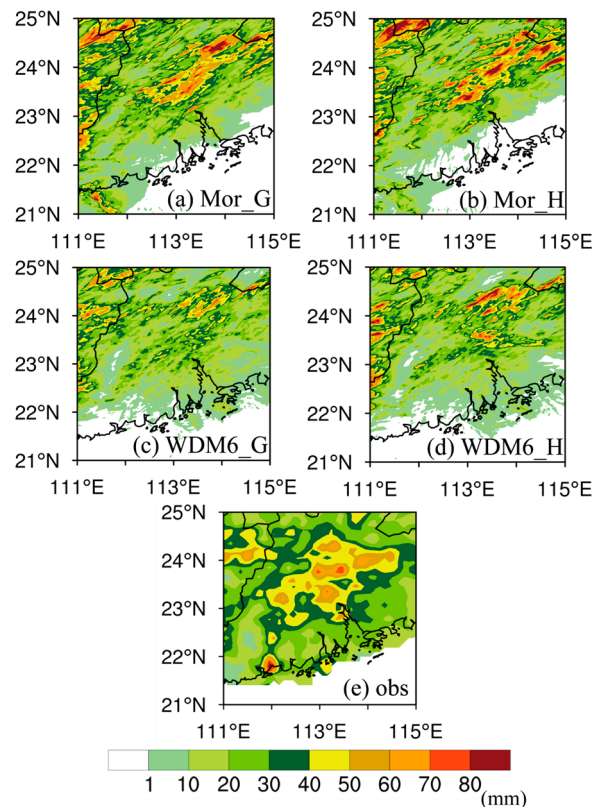
Figure 2. The spatial distribution of the 18-h accumulated surface precipitation for the 18-h period from 00:00 to 18:00 on 18 May, (**a**) represents the Mor_G scheme, (**b**) represents the Mor_H scheme, (**c**) represents the WDM6_G scheme, (**d**) represents the WDM6_H scheme, and (**e**) represents the observation from Chinese automatic surface stations with CMORPH retrievals.

We conducted a qualitative analysis of accumulated precipitation results for various schemes and will proceed with a detailed quantitative analysis. Taylor diagrams, which summarize the correlation between simulated and observed fields, are used to compare the performance of different simulation schemes [37]. To facilitate the comparison of simulation results with observational data by the Taylor diagram, the simulation results are interpolated onto the observed grid points (0.1° × 0.1°). Figure 3 shows the comparison results. The reference field is represented by observation data, with a correlation coefficient of 1.0 and a normalized standard deviation of 1.0. For the Mor_G scheme, the simulated correlation coefficient is 0.59 with a normalized standard deviation of 1.013. The Mor_H scheme has a correlation coefficient of 0.548 and a normalized standard deviation of 1.028. The WDM6_G scheme produces a correlation coefficient of 0.59 and a normalized standard deviation of 0.764, while the WDM6_H scheme results in a correlation coefficient of 0.52 and a normalized standard deviation of 0.921.
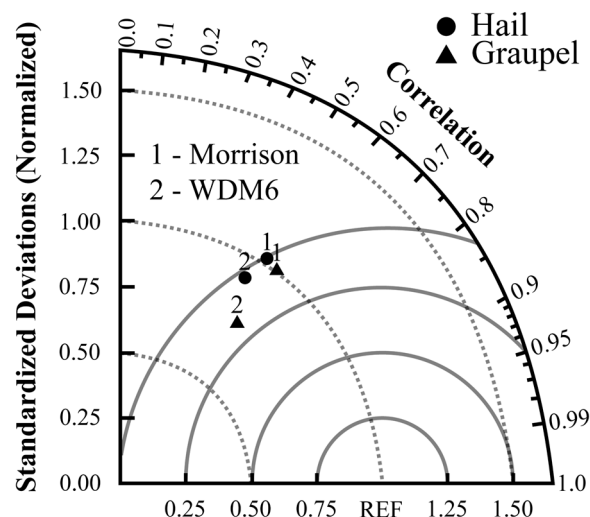
Figure 3. Taylor diagram for the 18-h accumulation rainfall for different schemes (the reference field is the observation from Chinese automatic surface stations with CMORPH retrievals, and normalized standard deviation is to normalize for the standard deviation by the standard deviation of the corresponding observed field).

The Mor_G and WDM6_G schemes show higher correlation coefficients than the Mor_H and WDM6_H schemes, indicating a better reproduction of overall rainfall spatial distribution. The Morrison schemes (Mor_G, Mor_H) have normalized standard deviations close to but slightly above 1, suggesting that they capture precipitation intensity trends reasonably well but slightly overestimate heavy rainfall. The average 18-h accumulated precipitation is 20.39 mm for the Mor_G scheme and 18.77 mm for the Mor_H scheme. Thus, the Mor_H scheme can effectively simulate cumulative precipitation, although it has a lower correlation coefficient due to positional deviations in heavy rainfall areas. In contrast, the WDM6_G scheme has an average precipitation of 14.75 mm, while the WDM6_H scheme averages 15.81 mm. Both WDM6 schemes significantly underestimate heavy rainfall, as evidenced by their lower average precipitation and normalized standard deviations well below 1. Despite the higher correlation coefficient of the WDM6_G scheme, its simulation of rainfall intensity remains inadequate. Overall, the Morrison schemes perform better than the WDM6 schemes, with Mor_G slightly outperforming Mor_H, and WDM6_H outperforming WDM6_G.

3.2. Evaluation of Radar Reflectivity and Polarization Variables

This study examines the mature stage of the convective system, which represents its peak intensity and greatest hazard. We selected the strongest domain-averaged hourly precipitation times for analysis by Figure 4: 10:00 for the Mor_G and Mor_H schemes and the observation, and 9:30 for the WDM6_G and WDM6_H schemes. Horizontal spatial distributions of radar reflectivity at different heights were compared between dual-polarization radar observations and simulations from all four schemes (Figure 5). All four schemes effectively simulated both the strong echo region areas with radar reflectivity ≥ 40 dBZ (hereafter referred to strong echo region) and the weak echo region corresponding to the trailing stratiform region (hereafter referred to as weak echo region).

The Mor_G and Mor_H schemes displayed broader radar reflectivity distributions than the WDM6_G and WDM6_H schemes. In the weak echo region, the radar reflectivity values and spatial distributions of Mor_G and Mor_H schemes were closer to observations. Below the 0 °C height level, except for the snow size in the Morrison scheme is larger than that in the WDM6 scheme between 3000–4000 m, there were no significant differences in both the number concentration and diameter of snow and graupel (hail) between the Morrison and WDM6 schemes in the weak echo region (Figures S1–S4). The primary variation in radar reflectivity arises from differences in raindrop values distribution. The

Mor_G scheme, which categorize rimed ice as graupel, simulate a wider but less intense strong echo region compared to the Mor_H scheme. Adams-Selin et al. found that graupel, with its slower fall velocity compared to hail, is more affected by updrafts, leading to a broader graupel distribution and a wider strong echo simulation [23]. This characteristic is less pronounced under 3000 m in the WDM6 simulations. This could be due to graupel particles in the WDM6_G scheme are almost completely melted at 3000 m (Figure S5), making it impossible for the scheme to simulate the characteristic of a broad distribution of graupel that leads to a widening of the strong radar reflectivity region.
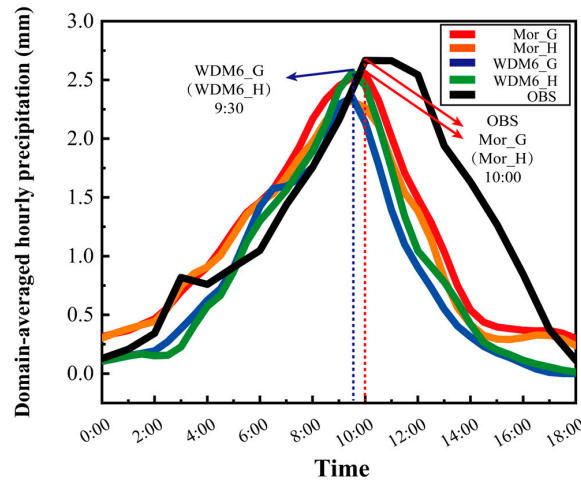
Figure 4. Domain-averaged hourly precipitation variation from 00:00 to 18:00 (UTC) over time. The red line represents the Mor_G scheme, orange line represents the Mor_H scheme, blue line represents the WDM6_G scheme, green line represents the WDM6_H scheme, and black line represents the observation from Chinese automatic surface stations with CMORPH retrievals.
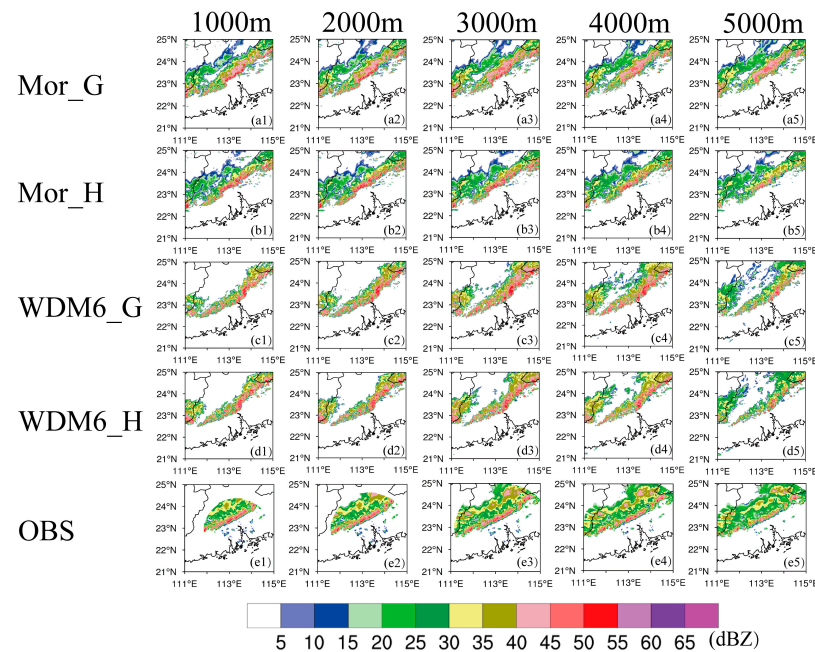

Figure 5. Horizontal cross-sections of radar reflectivity at different height, from left to right: 1000 m, 2000 m, 3000 m, 4000 m, and 5000 m. (**a1**–**a5**) represent the Mor_G scheme, (**b1**–**b5**) represent the Mor_H scheme, (**c1**–**c5**) represent the WDM6_G scheme, (**d1**–**d5**) represent the WDM6_H scheme, and (**e1**–**e5**) represent the observations.

Subsequently, by evaluating the radar polarimetric variables (Z_{DR} and K_{DP}) simulated by different schemes in Figures 6 and 7, we show that the Mor_G and Mor_H schemes produce spatial distributions of Z_{DR} and K_{DP} that more closely match the observations. Figure 6 shows horizontal cross-sections of K_{DP} at different heights. Observed K_{DP} values do not vary significantly with height. Strong echo regions of radar reflectivity exhibit a high K_{DP} value band, while weak echo regions show low K_{DP} values. In four simulations, K_{DP} values increase with decreasing height in strong echo areas, more pronounced in the Mor_G and Mor_H schemes. Compared to WDM6_G and WDM6_H, the Mor_G and Mor_H schemes simulate a wider and higher K_{DP} value band in strong echo regions, with increasing intensity and range as height decreases. These schemes also simulate lower K_{DP} values in the middle of weak echo regions. In contrast, the WDM6_G and WDM6_H schemes show a gradual decrease in K_{DP} values in this region. Below 3000 m, the K_{DP} values in these regions cannot be simulated. Overall, K_{DP} simulations in Mor_G and Mor_H are closer to observations.
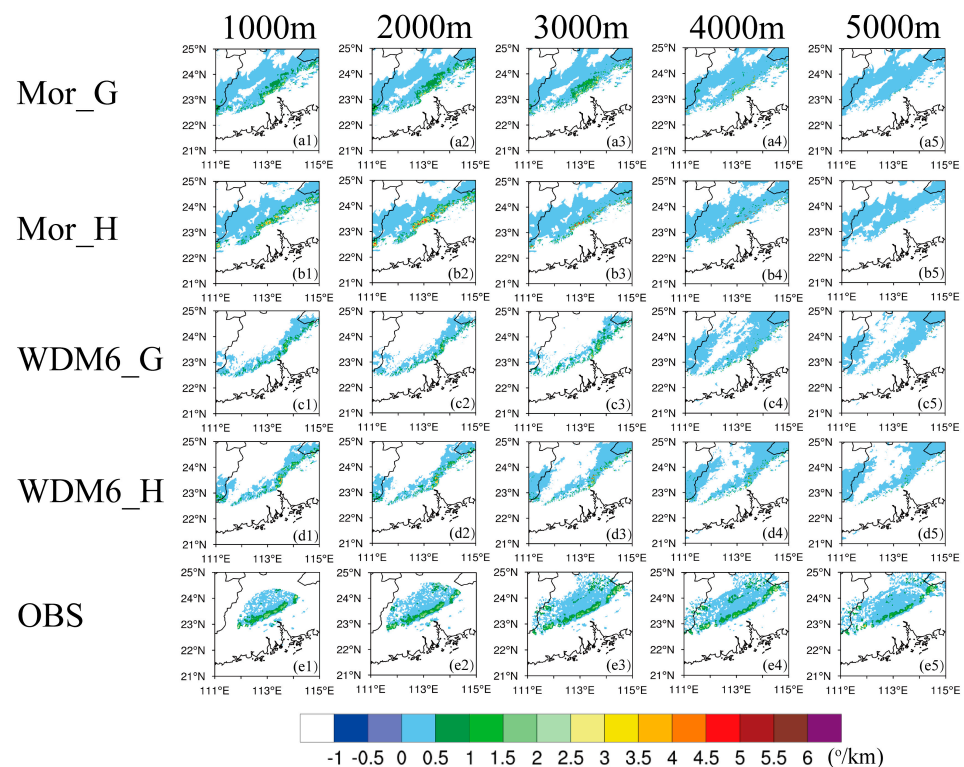

Figure 6. Same as Figure 5, but for the horizontal cross-sections of K_{DP} at different height levels.

Figure 7 presents horizontal cross-sections of Z_{DR} at various heights. High Z_{DR} values correspond to strong echo regions, with lower Z_{DR} values in the rear areas and decreasing range with the reduction in altitude. All simulations show increasing Z_{DR} values as height decreases, most notably in Mor_G and Mor_H. Simulations also depict a high Z_{DR} value band in strong echo regions at lower levels (1000–3000 m), weakening with a decrease in height. Mor_G and Mor_H significantly overestimate this band's intensity and extent, especially Mor_H. In weak echo regions, only Mor_G and Mor_H simulate Z_{DR} values, which are overestimated at lower levels.
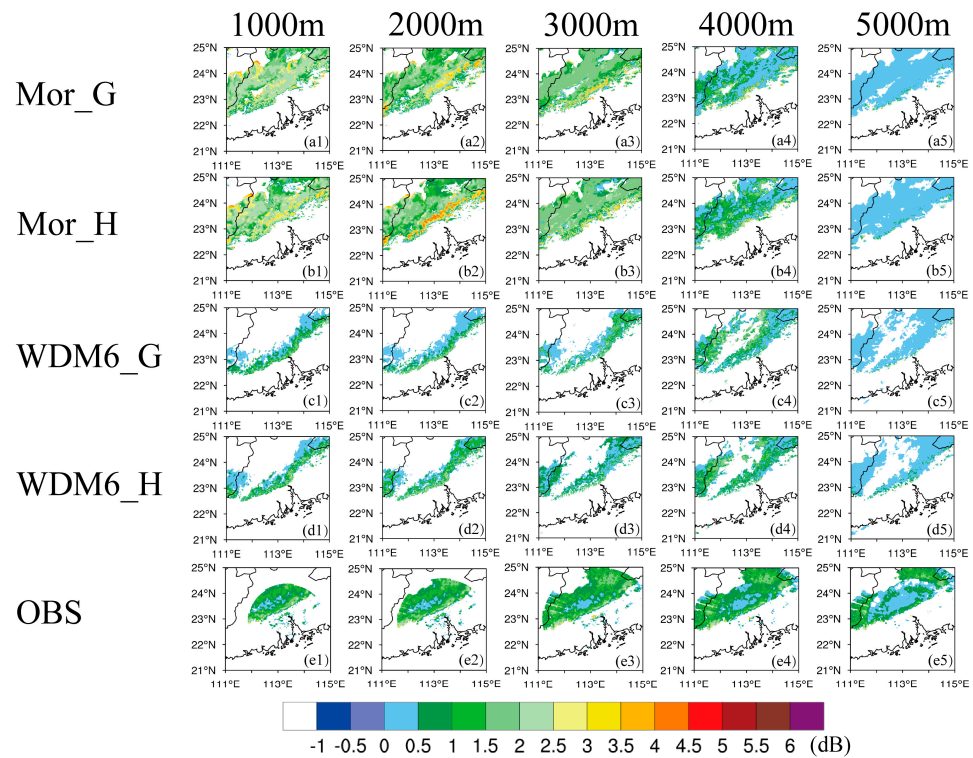
Figure 7. Same as Figure 5, but for the horizontal cross-sections of Z_{DR} at different height levels.

3.3. Evaluation of Spatial Distribution of Raindrop Diameters

Figure 8, presenting horizontal cross-sections of simulated raindrop mass-weighted diameters at various heights, as calculated by the PRD simulator, reveals that the differences of the values and spatial distribution of radar reflectivity, K_{DP}, and Z_{DR} between Morrison and WDM6 scheme are mostly influenced by the larger raindrop size in Morrison scheme.
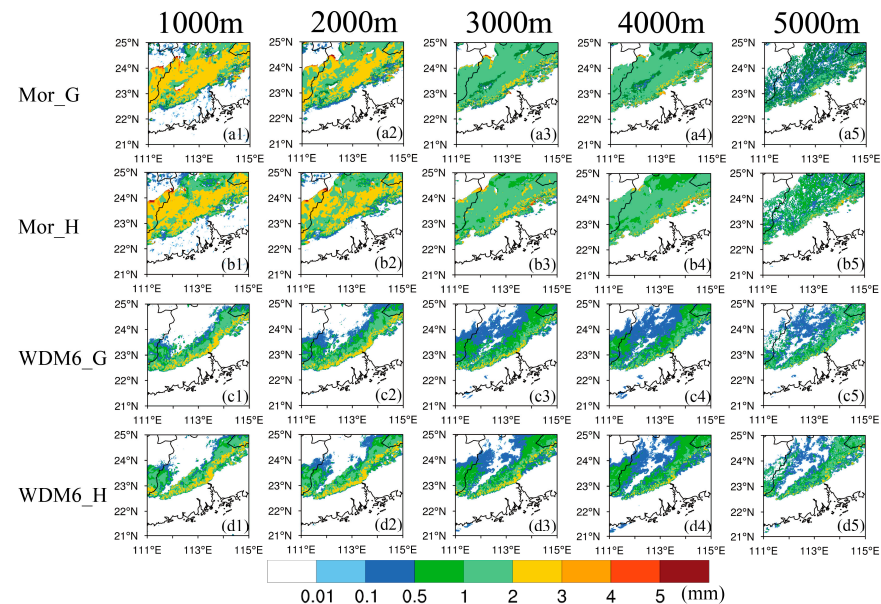
Figure 8. Horizontal cross-sections of raindrop mass-weighted diameters at different height levels, from left to right: 1000 m, 2000 m, 3000 m, 4000 m, and 5000 m. (**a1**–**a5**) represent the Mor_G scheme, (**b1**–**b5**) the Mor_H scheme, (**c1**–**c5**) the WDM6_G scheme and (**d1**–**d5**) the WDM6_H scheme.

In regions of strong echo, all four schemes simulate large raindrop sizes: between 2 and 4 mm at 1000–3000 m and 1–3 mm above 3000 m. This consistency allows all simula-

tions to represent high Z_{DR} values in strong echo regions. Conversely, in weak echo areas, raindrop diameters at 3000–4000 m reach 1–2 mm with the Mor_G and Mor_H schemes, whereas the WDM6_G and WDM6_H schemes mostly show diameters below 1 mm. At 1000–2000 m, Mor_G and Mor_H schemes predict larger diameters (2–4 mm), which may lead to an overestimation of Z_{DR} values. In contrast, the WDM6_G and WDM6_H schemes simulate very small raindrops that completely evaporate as the height decreases in the middle of the weak echo region, resulting in failures to simulate radar reflectivity and polarization variables. Zhou et al. also noted that the WDM6 schemes underestimate Z_{DR} due to smaller simulated raindrop sizes [31]. In all simulations, raindrop diameters increase with decreasing height, likely due to raindrop size sorting [12]. However, the WDM6_G and WDM6_H schemes capture this feature only in strong echo regions. Consequently, Z_{DR} increases with decreasing height for all simulations, but the WDM6_G and WDM6_H schemes only perform well in strong echo areas.

K_{DP} is influenced by both raindrop diameter and the distribution of raindrop number concentration. Figure 9 shows the spatial distribution of simulated raindrop number concentration. In the Morrison scheme, a band of high raindrop number concentration appears in the strong echo region, while the number concentration is lower in the weak echo region. This distribution corresponds more closely with the characteristics of high K_{DP} values, particularly below 3000 m. Moreover, there is little difference in raindrop size between the strong and weak echo regions below this height. For the WDM6 schemes, raindrop number concentration shows little variation between strong and weak echo regions, but raindrop diameter is larger in the strong echo regions, aligning with the K_{DP} values distribution. Thus, the K_{DP} values distribution in the Morrison schemes are more closely linked to raindrop number concentration, especially below 3000 m. In the WDM6 schemes, K_{DP} distribution is primarily driven by raindrop diameter.
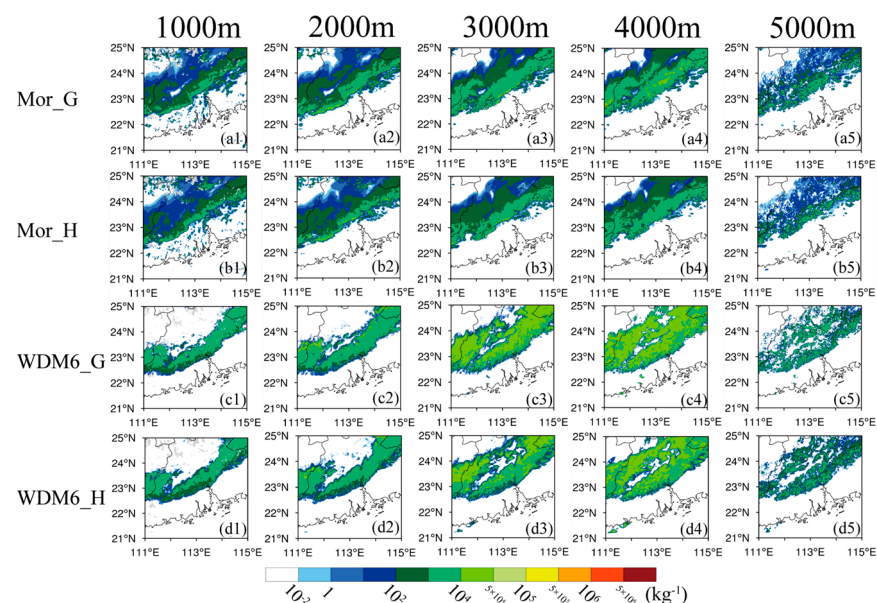

Figure 9. Same as Figure 8, but for the horizontal cross-sections of raindrop number concentration at different height levels.

The choice of rimed ice category (graupel for Mor_G and WDM6_G, hail for Mor_H and WDM6_H) has minimal impact on simulated raindrop sizes below freezing, resulting in similar spatial distributions of accumulated precipitation. Bryan and Morrison, and Weverberg et al., also found that sensitivity to rimed ice category is low in idealized squall line simulations [22,26]. While, in this convective event, significant differences in raindrop diameters between double-moment (Mor_G and Mor_H) and partially double-moment (WDM6_G and WDM6_H) schemes result in variations in precipitation distribution.

3.4. The Microphysical Processes and Parameters Related to Rain Production

From Figure 10, which is the probability density functions (PDFs) of raindrop mass mixing ratio, number concentration, and mass-weighted diameter with height, we investigate that the key causes of differences in raindrop size are rain number concentration. The WDM6_G and WDM6_H schemes simulate raindrops with diameters exceeding 2 mm above the 0 °C height level, whereas in the Mor_G and Mor_H schemes, most raindrops are smaller than 1 mm. Below the 0 °C height level, raindrop diameters are generally larger in the Mor_G and Mor_H schemes compared to the WDM6_G and WDM6_H schemes, with a more pronounced increase in diameter with decreasing height in the former. Despite similar distributions of raindrop mixing ratio below the 0 °C height level across simulations, the number concentration is significantly higher in the WDM6_G and WDM6_H schemes than in the Mor_G and Mor_H schemes. This difference is likely due to the varying number concentrations of raindrops below the 0 °C height level.
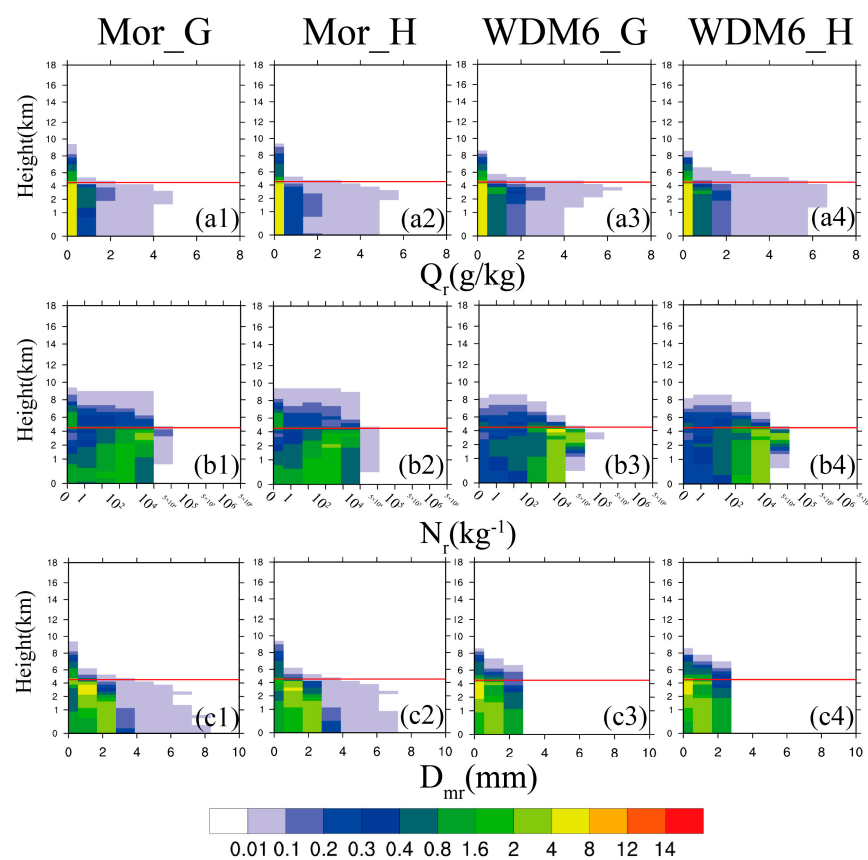

Figure 10. PDFs of raindrop microphysical variables for the Mor_G, Mor_H, WDM6_G, and WDM6_H schemes from left to right. The red line represents the average height of the 0 °C height level across all grid points. (**a1**–**a4**) represent the PDF of raindrop mass mixing ratio, (**b1**–**b4**) represent the PDF of raindrop number concentration, and (**c1**–**c4**) represent the PDF of raindrop mass-weighted diameter.

By analyzing the mass mixing ratio and number concentration conversion rates for raindrop source/sink terms (details in Table A1) across all four schemes shown in Figure 11, we can investigate the reasons for differences in raindrop number concentration below the 0 °C height level. The primary contributor to the sink terms for raindrop mass mixing ratio in all schemes is evaporation. The source terms are mainly influenced by the melting of snow and graupel/hail and the collection of cloud droplets by raindrops. In the Mor_G and WDM6_G schemes, graupel melting contributes more to raindrop mass mixing ratio than snow melting. In the Mor_H and WDM6_H schemes, hail's higher fall speed and a longer distance of melting allows it to survive in a lower height, contributing to stronger radar reflectivity and explaining the increased extent and intensity of the strong echo region.
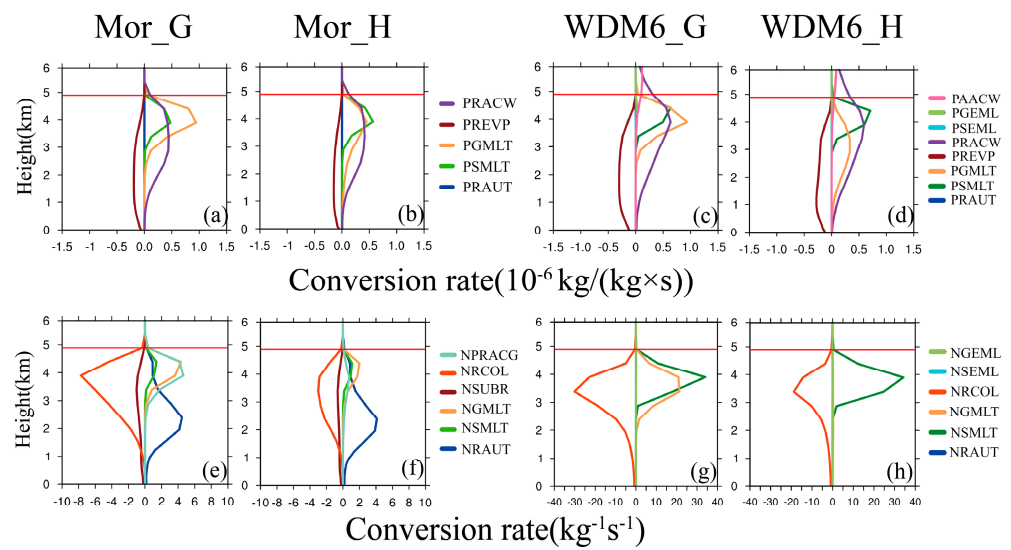
Mor_G   Mor_H   WDM6_G   WDM6_H

Figure 11. Mixing ratio and number concentration conversion rate related to source and sink terms of raindrop for the Mor_G, Mor_H, WDM6_G, and WDM6_H schemes from left to right. The red line represents the average height of the 0 °C height level across all grid points. (**a–d**) represent the mass mixing ratio conversion rate, and (**e–h**) represent the number concentration conversion rate.

In all schemes, the sink terms for raindrop number concentration are primarily due to raindrop self-collection. For the source terms, the Mor_G and Mor_H schemes are mainly influenced by the shedding of melting raindrops from graupel/hail, auto-conversion of cloud water to rain, and the melting of graupel/hail and snow. Conversely, in the WDM6_G and WDM6_H schemes, the primary contributions come from the melting of graupel/hail and snow. Raindrop self-collection is sensitive to the rimed ice category (graupel or hail), with a more pronounced decrease in raindrop number concentration below the 0 °C height level in the Mor_G and WDM6_G schemes compared to the Mor_H and WDM6_H schemes. This is likely due to higher simulated raindrop concentrations in Mor_G and WDM6_G compared to Mor_H and WDM6_H. Snow melting is more significant in the WDM6_G and WDM6_H schemes than in the Mor_G and Mor_H schemes, while cloud-to-rain auto-conversion is lower in WDM6_G and WDM6_H, indicating more cloud droplets are converted to raindrops in the Mor_G and Mor_H schemes between 3000 and 1000 m. The melting of graupel/hail contributes significantly more to raindrop number concentration in the WDM6_G scheme compared to Mor_G and Mor_H, and is minimal in the WDM6_H scheme due to the larger size and lower number concentration of hail. Overall, the differences in raindrop number concentration below the 0 °C height level among the four schemes are primarily due to variations in the contribution of ice-phase particle melting.

The melting of ice-phase precipitation particles is governed by different melting parameterizations in the various schemes (details are in Appendix A). The number concentration of raindrops generated by the melting of these particles is proportional to the raindrop mixing ratio. Unlike the Morrison schemes (which use a double-moment approach for ice particles), the WDM6 schemes (using a single-moment approach) represent the relationship between raindrop number concentration and mixing ratio through the ratio of the intercept parameter (N_0) to the slope parameter (λ) of ice-phase particles. Consequently, the λ and N_0 values for snow and graupel/hail in the WDM6 scheme influence the raindrop number concentration produced by melting.

Building on these insights, we analyzed the differences in λ and N_0 for snow and graupel between the Morrison and WDM6 schemes, and discussed how these differences affect the melting processes in each scheme. Figures 12 and 13 illustrate the PDFs of λ and N_0 for snow and graupel/hail across the four schemes. Above the 0 °C height level, λ for snow is lower in the Mor_G and Mor_H schemes compared to the WDM6_G and WDM6_H

schemes. As height approaches the 0 °C height level, the differences between the Morrison and WDM6 schemes diminish. Both schemes show a decreasing trend in N_0 for snow with the reduction in altitude. For graupel/hail, λ values are similar between the Mor_G, Mor_H, WDM6_G, and WDM6_H schemes, but N_0 is higher in the Morrison schemes, leading to slower fall speeds and enhanced growth conditions for graupel/hail [38].
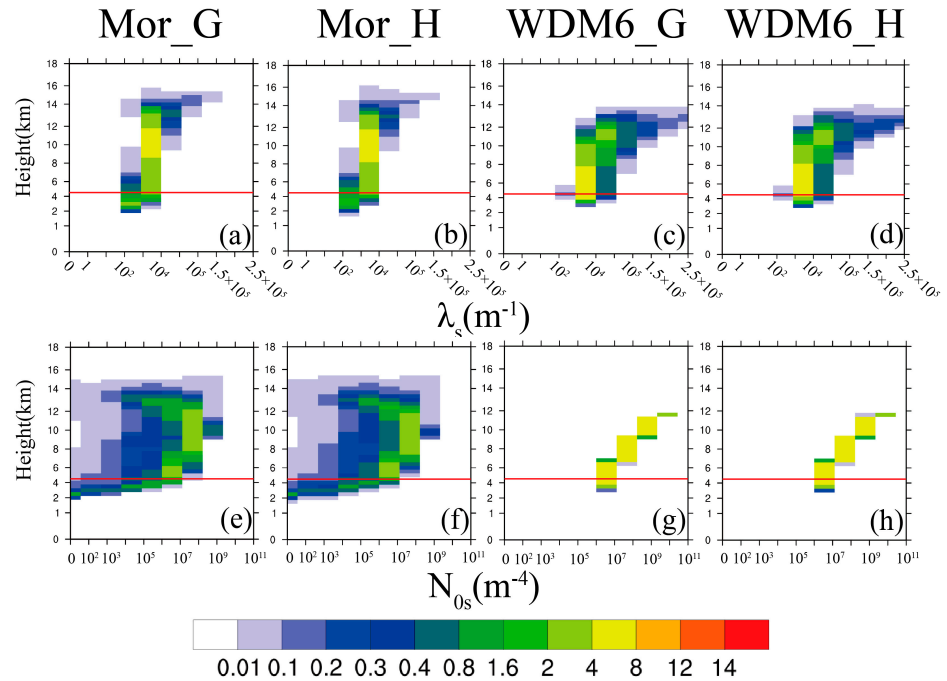

Figure 12. Particle size distribution parameters of snow for the Mor_G, Mor_H, WDM6_G, and WDM6_H schemes from left to right. The red line represents the average height of the 0 °C height level across all grid points. (**a**–**d**) represent the PDF distribution of snow λ, and (**e**–**h**) represent the PDF distribution of snow N_0.
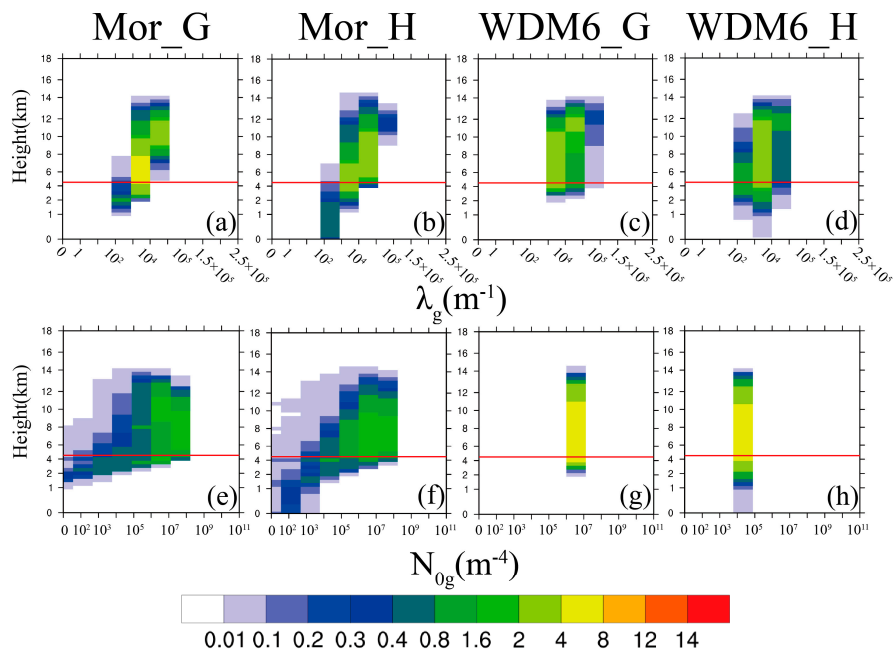
Figure 13. Same as Figure 12, the particle size distribution parameters for graupel/hail.

Below the 0 °C height level, λ for snow and graupel/hail decreases with the reduction in height in the Mor_G and Mor_H schemes but remains unchanged in the WDM6_G and WDM6_H schemes. Despite these changes, the λ values are similar between the Morrison and WDM6 schemes. There are significant differences in the N_0 values: in the Morrison schemes, N_0 for snow and graupel/hail decreases notably as the height drops, while in the WDM6 schemes, N_0 remains constant.

3.5. Sensitivity Experiment Results

Differences in N_0 values for snow and graupel/hail particles between the Morrison (Mor_G and Mor_H) and WDM6 (WDM6_G and WDM6_H) schemes may influence melting processes, leading to significant variations in raindrop concentration and diameter, and thus affecting simulated precipitation. We designed two sets of sensitivity experiments to investigate the impact of N_0 settings for snow (N_{0s}) and graupel/hail ($N_{0g/h}$) in the WDM6 scheme on precipitation simulation. The N_{0s} decreases with temperature and is defined as a function with a constant of 2×10^6 m^{-4} (the equation can be found in Appendix A. The N_{0g}, set at 4×10^6 m^{-4} for graupel and 4×10^4 m^{-4} for hail. They were adjusted by a factor of 10. Figures 14 and 15 show the conversion rates for raindrop mass mixing ratio and number concentration in these tests. Changes in N_{0s} had minimal impact on raindrop mass mixing ratios. However, decreasing/increasing N_{0s} similarly affected snow melting contributions to raindrop concentration and reduced raindrop self-collection, with a more pronounced effect in the WDM6_H scheme.
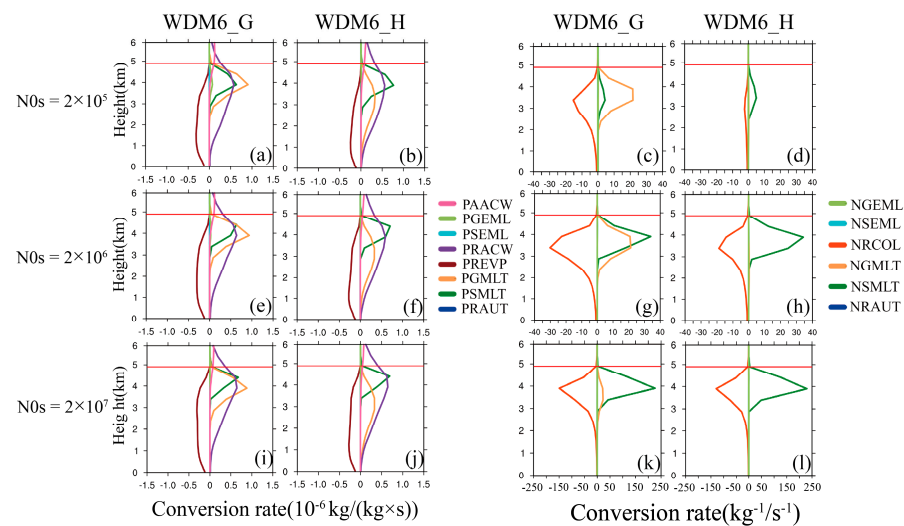

Figure 14. Left two columns are mixing ratio conversion rate related to source and sink terms of raindrop for WDM6_G and WDM6_H schemes, while right two columns are number concentration conversion rate related to source and sink terms of raindrop. The red line represents the average height of the 0 °C height level across all grid points. (**a–d**) represent the experiment with $N_{0s} = 2 \times 10^5$ m^{-4}, (**e–h**) represent the original simulation with $N_{0s} = 2 \times 10^6$ m^{-4}, (**i–l**) represent the experiment with $N_{0s} = 2 \times 10^7$ m^{-4}.

Reducing N_{0g} decreased the contribution of graupel/hail melting to raindrop mass mixing ratios between the 0 °C height level and 2000 m, causing graupel/hail to melt at lower levels. Lowering N_{0g} also weakened the processes of graupel/hail melting and raindrop self-collection in both WDM6_G and WDM6_H schemes, with a smaller effect in WDM6_H. Conversely, increasing N_{0g} significantly increased these contributions in the WDM6_G scheme, while the change in the contribution of hail melting to raindrop number concentration for WDM6_H was consistent with WDM6_G but relatively small due to lower hail concentration. Raindrop self-collection remained almost unchanged in the WDM6_H sensitivity experiments for N_{0g}.
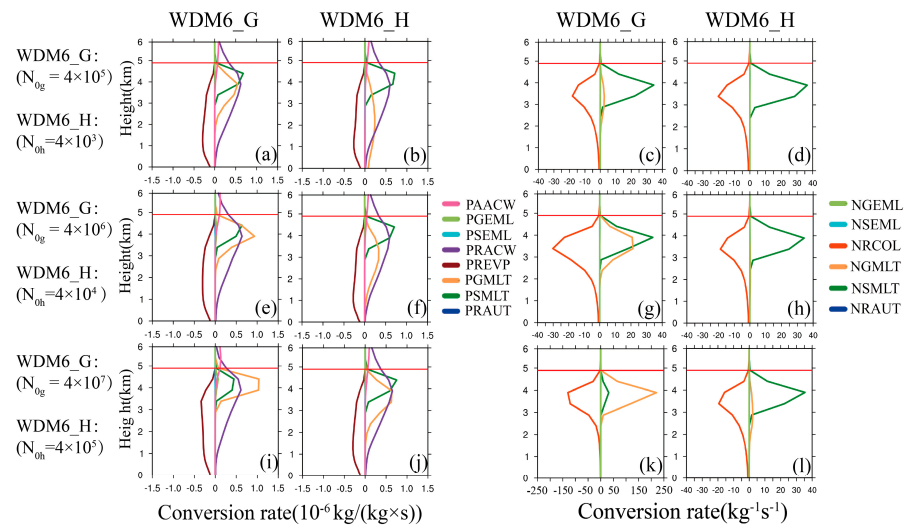
Figure 15. Same as Figure 14. (**a–d**) represent the experiment with $N_{0g} = 4 \times 10^5$ m^{-4}/$N_{0g} = 4 \times 10^3$ m^{-4}, (**e–h**) represent the original simulation $N_{0g} = 4 \times 10^6$ m^{-4}/$N_{0h} = 4 \times 10^4$ m^{-4}, (**i–l**) represent the experiment with $N_{0g} = 4 \times 10^7$ m^{-4}/$N_{0h} = 4 \times 10^5$ m^{-4}.

To further investigate the effects of varying N_0 for snow and graupel/hail on raindrop number concentration and diameter, Figures 16 and 17 show the differences in PDF distributions between the sensitivity experiments and the original simulations. For the WDM6_G scheme, decreasing N_{0s} mainly affects the 2000–4000 m range, where the proportion of raindrop concentrations between 10–10^3 kg^{-1} increases while concentrations above 10^3 kg^{-1} decrease. The proportion of raindrops with a mass-weighted diameter between 1 and 2 mm slightly increases. In contrast, for the WDM6_H scheme, decreasing N_{0s} results in reduced raindrop number concentration below the 0 °C height level, with a more pronounced decrease with the reduction in altitude. Between 2000 and 4000 m, the proportion of raindrops with a mass-weighted diameter below 1 mm decreases, while the proportion with diameters between 1 and 2 mm increases.
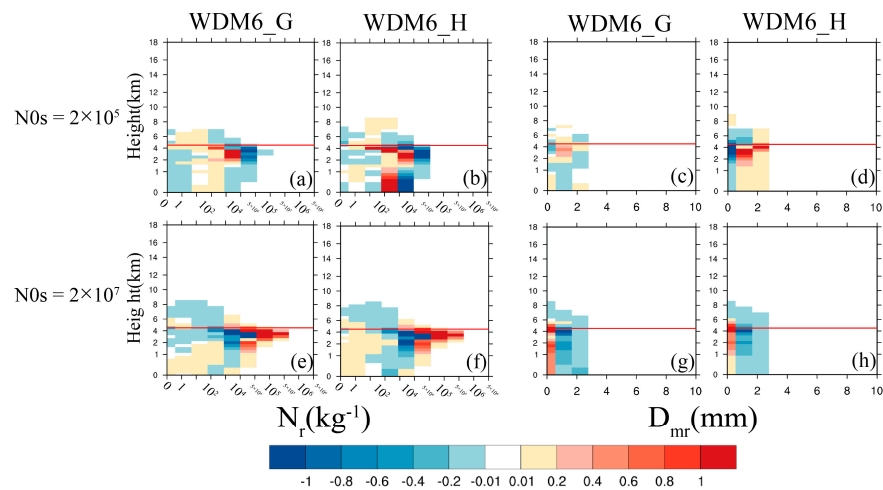

Figure 16. Left two columns display raindrop number concentration of WDM6_G and WDM6_H schemes. Figures show the difference in PDF between the sensitivity experiment and the original simulation result with unmodified N_0. While the right two columns present same comparisons for the raindrop mass-weighted diameter. The red line represents the average height of the 0 °C height level across all grid points. (**a–d**) show the differences when $N_{0s} = 2 \times 10^5$ m^{-4} minus the original simulation result with $N_{0s} = 2 \times 10^6$ m^{-4}, (**e–h**) represent the experiment with $N_{0s} = 2 \times 10^7$ m^{-4} minus the original simulation result.
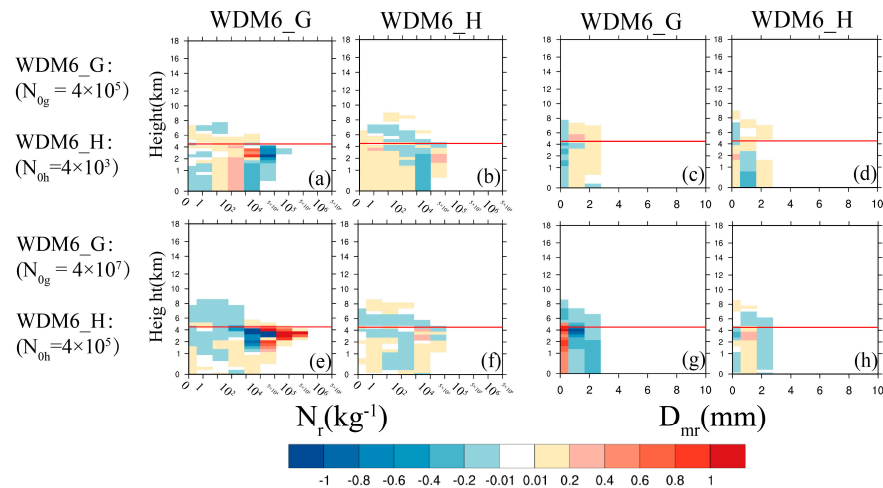
Figure 17. Same as Figure 16. (**a**–**d**) represent the experiment with $N_{0g} = 4 \times 10^5$ m^{-4}/$N_{0h} = 4 \times 10^3$ m^{-4}, (**e**–**h**) represent the experiment with $N_{0g} = 4 \times 10^7$ m^{-4}/$N_{0h} = 4 \times 10^5$ m^{-4}.

Increasing N_{0s} leads to a significant rise in raindrop number concentration in the 2000–4000 m range for both schemes, while the effect diminishes below 2000 m. Overall, the proportion of raindrop concentrations exceeding 10^3 kg^{-1} increases. For the WDM6_G scheme, the proportion of raindrops with a mass-weighted diameter below 1 mm increases more noticeably below 2000 m compared to the WDM6_H scheme.

Meanwhile, decreasing N_{0g} leads to a reduction in the proportion of raindrop concentrations between 10^3 and 10^4 kg^{-1} below 1 km for both WDM6_G and WDM6_H schemes, while increasing the proportion between 10^2 and 10^3 kg^{-1} in the WDM6_G scheme. Changes in raindrop diameter are minimal for both schemes. In the WDM6_G scheme, the proportion of raindrops with diameters below 1 mm decreases, whereas in the WDM6_H scheme, the proportion of diameters between 0 and 2 mm decreases. The WDM6_G scheme shows a slight increase in diameters between 1 and 2 mm, while the WDM6_H scheme shows an increase in diameters over 2 mm. Increasing N_{0g} in the WDM6_G scheme results in a more significant increase in raindrop number concentration exceeding 10^4 kg^{-1} and a decrease between 10^2 and 10^3 kg^{-1} in the 2000-4000 m range compared to the WDM6_H scheme. The proportion of raindrops with diameters below 1 mm increases significantly in the WDM6_G scheme, with no significant changes in the WDM6_H scheme.

In summary, decreasing N_{0s} leads to a more pronounced increase in raindrop size in the WDM6_H scheme compared to the WDM6_G scheme. However, raindrop size changes are not significant in either scheme when N_{0g} decreases. Conversely, an increase in N_{0g} causes a more significant decrease in raindrop diameter in the WDM6_G scheme compared to the WDM6_H scheme.

Finally, Figure 18 illustrates the 18-h accumulated surface precipitation for various sensitivity experiments, which indicates that altering N_{0s} has a more significant effect on the spatial distribution of precipitation than changing N_{0g}. In the WDM6_G scheme, decreasing N_{0s} or N_{0g} increases the extent of precipitation exceeding the severe rainfall level, with a more pronounced effect when N_{0s} is reduced. Additionally, reducing N_{0s} results in the simulation of more extreme heavy rainfall regions. Conversely, increasing N_{0s} or N_{0g} reduces the precipitation area above the severe level, with a more noticeable decrease when N_{0s} is increased.
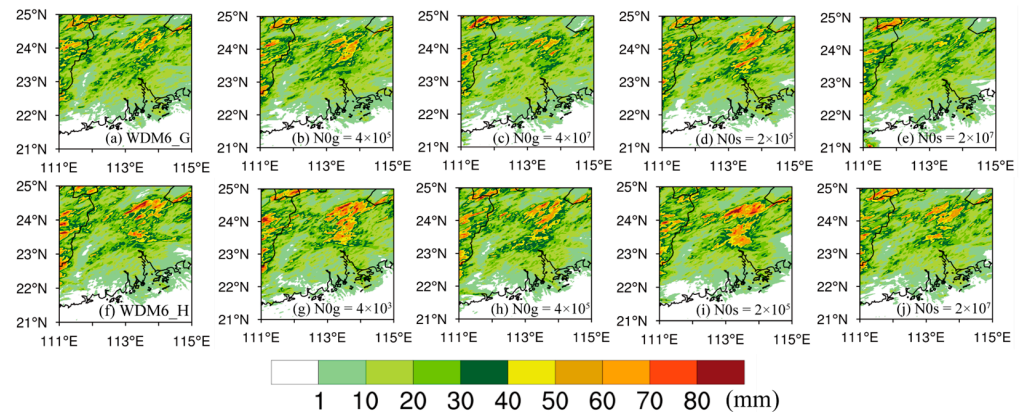
Figure 18. The spatial distribution of 18-h accumulated surface precipitation. (**a**) represents the original WDM6_G simulation results ($N_{0s} = 2 \times 10^6$ m^{-4}, $N_{0g} = 4 \times 10^6$ m^{-4}), (**b**–**e**) represent simulation results of WDM6_G under different under different sensitivity experiments. (**b**) represents the results with $N_{0s} = 2 \times 10^6$ m^{-4}, $N_{0g} = 4 \times 10^5$ m^{-4}, (**c**) represents the results with $N_{0s} = 2 \times 10^6$ m^{-4}, $N_{0g} = 4 \times 10^7$ m^{-4}, (**d**) represents the results with $N_{0s} = 2 \times 10^5$ m^{-4}, $N_{0g} = 4 \times 10^6$ m^{-4}, (**e**) represents the results with $N_{0s} = 2 \times 10^7$ m^{-4}, $N_{0g} = 4 \times 10^6$ m^{-4}. (**f**) represents the original WDM6_H simulation results ($N_{0s} = 2 \times 10^6$ m^{-4}, $N_{0g} = 4 \times 10^4$ m^{-4}), (**g**–**j**) represent simulation results of WDM6_H under different under different sensitivity experiments.

For the WDM6_H scheme, decreasing N_{0s} or N_{0g} also enlarges the precipitation areas above the severe level, particularly increasing extreme heavy rainfall regions, especially when N_{0s} is reduced. However, increasing N_{0s} or N_{0g} has minimal impact on the extent of precipitation above the severe level, but decreases the extreme heavy rainfall areas, with a more significant reduction when N_{0s} is increased compared to changes in N_{0g}.

4. Discussion

Based on the study, it was found that the simulated spatial distributions of radar reflectivity, Z_{DR}, and K_{DP} are linked to raindrop size and number concentration simulations. The Mor_G and Mor_H schemes produce a broader distribution of radar reflectivity and a greater coverage of weak echo regions compared to the WDM6_G and WDM6_H schemes. However, the Mor_G and Mor_H schemes tend to overestimate raindrop diameters, leading to higher Z_{DR} values in some areas. Conversely, the WDM6_G and WDM6_H schemes simulate smaller raindrops in weak echo regions (4000–3000 m), resulting in negligible K_{DP} and Z_{DR} values at these heights and below. Zhou et al. and Wu et al. have also noted that the Morrison scheme's larger Z_{DR} values are due to an overestimation of average raindrop diameters [31,39], while the WDM6 scheme's smaller Z_{DR} values result from a higher concentration of small and medium-sized raindrops [40,41].

We analyze the causes of differences in raindrop size distributions between the Morrison and WDM6 schemes. Wu et al. attributed the Morrison scheme's overestimation of raindrop diameter to an underestimation of pristine ice particle concentration, while the WDM6 scheme's more active warm rain processes result in smaller raindrop diameters [39]. However, our analysis of precipitation in Guangdong on 8 May 2017, attributes the WDM6 scheme's overestimation of raindrop concentration and underestimation of raindrop diameter to the fixed N_0 for ice-phase particles below the 0 °C height level.

Additionally, schemes using graupel as the rimed ice category (Mor_G and WDM6_G) simulate a broader range of strong echo regions but with lower intensity, mainly due to the slower fall speed of graupel [5]. In contrast, larger and heavier hail, which fall out of the updraft earlier, result in less melting and evaporation, thus concentrating rainfall in the convective precipitation band [23].

The research also indicated the choice of rimed ice phase particles has a little impact on real-case precipitation studied in this work. Bryan and Morrison demonstrated that precipitation is minimally sensitive to the rimed ice category in idealized squall line simulations

using the M-Y scheme [22]. Similarly, Weverberg et al. found that the rimed ice category has little influence on precipitation in both Morrison and M-Y scheme simulations [26]. For this study on real case, whether graupel or hail represents rimed ice particles has a minor effect on raindrop size distribution below the 0 °C height level, making the spatial distribution of cumulative precipitation less sensitive to the rimed ice category.

Figures 19 and 20 show the affected microphysical processes and the changes in various microphysical variables in the sensitivity experiments for $N_{0s(g/h)}$ of snow (graupel/hail).
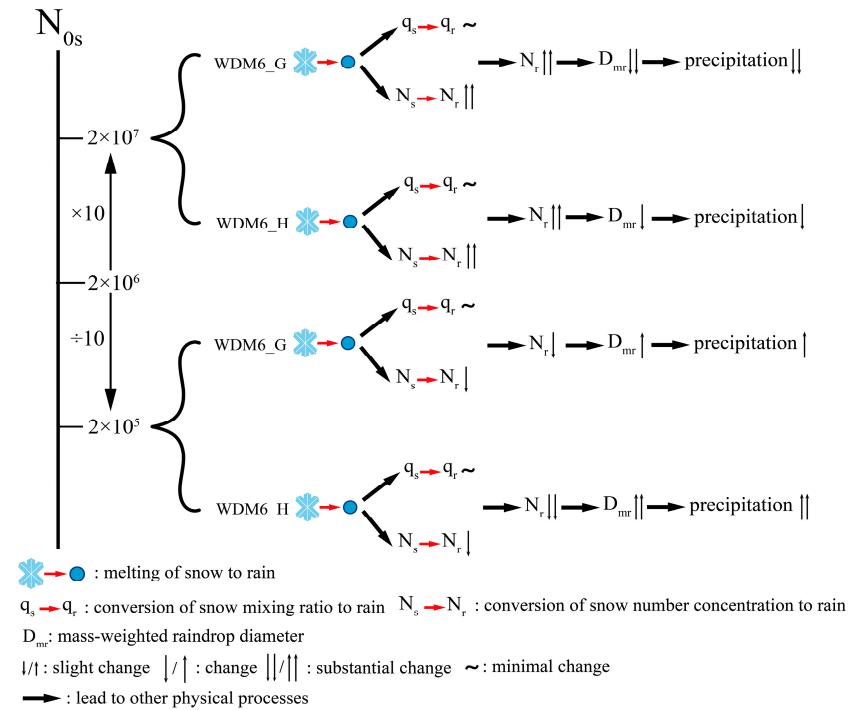
Figure 19. Microphysical processes influenced by snow N_{0s} in sensitivity experiment of WDM6_G and WDM6_H scheme.
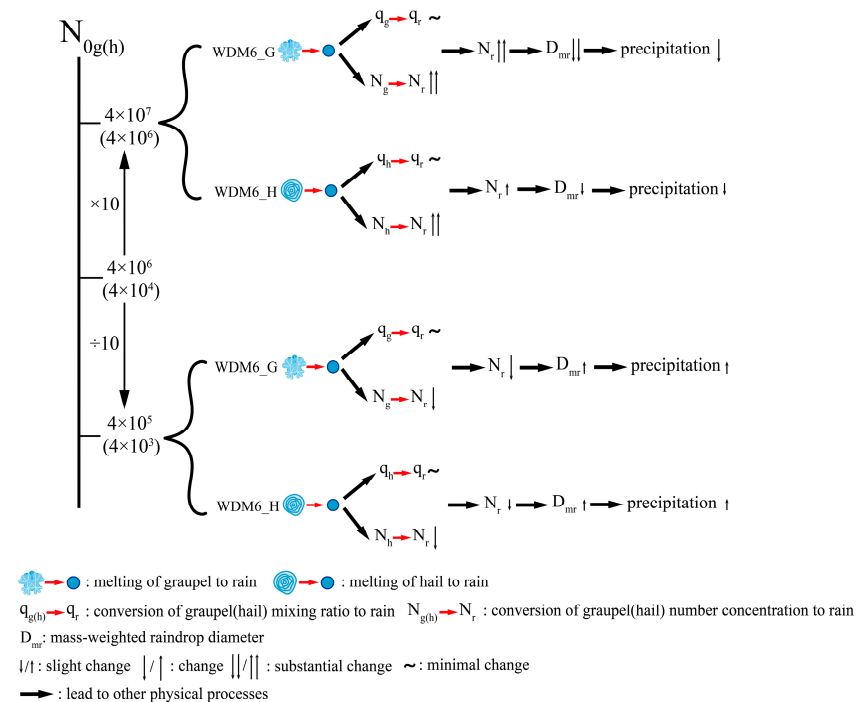
Figure 20. Same as Figure 19, microphysical processes results of graupel/hail $N_{0g/h}$.

5. Conclusions

Four "bulk" microphysics schemes were used to simulate a severe convective precipitation event in Guangdong from May 7 to 8, 2017. These schemes include the Morrison scheme with graupel and hail representing rimed ice particles (Mor_G, Mor_H) and the WDM6 scheme with similar representations (WDM6_G, WDM6_H). The simulations were evaluated based on polarimetric observations and PRD simulator results. The study assessed how the choice between single-moment and double-moment ice microphysics schemes, and the rimed ice category (graupel or hail), affects convective precipitation simulations. Key findings include:

1. All schemes underestimated overall precipitation intensity and the extent of severe rainfall areas. The Mor_G and Mor_H schemes predicted larger and more concentrated severe rainfall areas compared to WDM6_G and WDM6_H. Additionally, Mor_G and Mor_H simulated more extreme heavy rainfall areas than observed.
2. Significant differences in the distribution of mass-weighted raindrop diameter with height were simulated based on the choice of single-moment or double-moment ice-phase schemes. These differences impacted the spatial distribution of cumulative precipitation, primarily due to variations in raindrop concentration below the 0 °C height level, influenced by ice-phase melting processes. The N_0 values for snow and graupel/hail in the WDM6 scheme affected the melting contributions to raindrop concentration.
3. Sensitivity experiments on the WDM6_G and WDM6_H schemes showed that reducing N_{0s} or N_{0g} increased precipitation areas above severe rainfall levels, with more significant effects in the N_{0s} reduction experiment. Increasing N_{0s} or N_{0g} had the opposite effect, more pronounced in the N_{0s} increase experiment. For WDM6_H, reducing N_{0s} or N_{0g} also expanded precipitation areas above severe rainfall levels, with more substantial changes in the N_{0s} reduction experiment. However, increasing N_{0s} or N_{0g} did not significantly affect precipitation areas above severe levels but reduced extreme heavy rainfall areas, with a larger effect in the N_{0s} increase experiment.

This study demonstrated that altering the assumed N_0 for ice-phase precipitation particles does not significantly impact the simulation of cumulative precipitation for light to moderate rainfall levels. Further research is required to explore factors affecting precipitation intensity in these ranges. Additionally, while this study examined the effects of microphysical processes on convective precipitation simulations, it did not address the influence of dynamical processes. These aspects should be investigated in future studies. Furthermore, this research focused on a single real-case event using only the Morrison and WDM6 schemes. Future studies should analyze multiple cases across different times and regions and incorporate the triple-moment microphysics schemes [42,43].

Appendix A

Appendix A.1. Introduction of Microphysical Schemes

Appendix A.1.1. WDM6 Scheme

The WDM6 scheme is the extended version of the WSM6 which adds the prognostic number concentration of cloud and rainwater together with the cloud condensation nuclei (CCN). The WDM6 scheme predicts the mass mixing ratios of cloud droplets, raindrops, ice crystals, snowflakes, and graupel/hail, but it only predicts the number concentrations of cloud droplets, raindrops, and CCN [19]. In the WDM6 scheme, the cloud–raindrop size distributions are assumed to follow the normalized form. The ice-phase microphysics of WDM6 scheme is same as WSM6 scheme. Snow and graupel/hail are assumed to have Marshall-Palmer (M-P) size distributions of the form. The intercept parameter for snow (N_{0s}) is defined as a formula increased as the temperature decreases [44], which can be expressed as:

$$N_{0s}(m^{-4}) = 2 \times 10^6 \times e^{[0.12(T_0 - T)]} \tag{A1}$$

The intercept parameter for graupel/hail (N_{0g}/N_{0h}) is assumed as a constant [45].

Appendix A.1.2. Morrison Scheme

The two-moment microphysics scheme which is based on the parameterization of Morrison et al. [11] implemented into WRF predicts the mass mixing ratios and number concentrations of five hydrometeor species: cloud droplets, cloud ice, snow, rain, and graupel/hail. The cloud and precipitation particle size distributions are represented by gamma functions.

Appendix A.2. Introduction of Melting Schemes

In the Morrison scheme, when calculating the changes in the number concentration of snow and graupel/hail due to melting, it is assumed that the changes in number concentration are proportional to the changes in mass mixing ratio caused by melting. It is shown in Equation (A2):

$$N_{x(mlt)}(m^{-3}s^{-1}) = \frac{q_{x(mlt)}}{q_x} \times N_x \tag{A2}$$

In the WDM6 scheme, the change in the number concentration of snow and graupel/hail due to melting is given by Equation (A3).

$$N_{x(mlt)}(m^{-3}s^{-1}) = \frac{q_{x(mlt)}}{q_x} \times \frac{N_{0x}}{\lambda_x} \tag{A3}$$

Appendix B

Table A1. Sources and sinks of raindrop mass mixing ratio and number concentration below the 0 °C height level.

	Abbreviation	Description
Production ratio for mixing ratio	PAACW	Accretion of cloud water by averaged snow/graupel
	PGEML	Enhanced melting of graupel by accretion of water in the WDM6 scheme
	PSEML	Enhanced melting of snow by accretion of water in the WDM6 scheme
	PRACW	Collection of cloud water by rain
	PREVP	Evaporation of rain
	PGMLT	Melting of graupel to rain
	PSMLT	Melting of snow to rain
	PRAUT	Auto-conversion of cloud droplets to rain
Production ratio for number concentration	NPRACG	Shedding of graupel in the Morrison scheme
	NSUBR	Evaporation of rain
	NGEML	Enhanced melting of graupel by accretion of water in the WDM6 scheme
	NSEML	Enhanced melting of snow by accretion of water in the WDM6 scheme
	NRCOL	Self-collection and break-up of rain-drops
	NGMLT	Melting of graupel to rain
	NSMLT	Melting of snow to rain
	NRAUT	Auto-conversion of cloud droplets to rain

References

1. Doswell, C.A. Severe Convective Storms in the European Societal Context. *Atmos. Res.* **2015**, *158–159*, 210–215. [CrossRef]
2. Zhou, K.; Zheng, Y.; Li, B.; Dong, W.; Zhang, X. Forecasting Different Types of Convective Weather: A Deep Learning Approach. *J. Meteorol. Res.* **2019**, *33*, 797–809. [CrossRef]
3. Köcher, G.; Zinner, T.; Knote, C.; Tetoni, E.; Ewald, F.; Hagen, M. Evaluation of Convective Cloud Microphysics in Numerical Weather Prediction Models with Dual-Wavelength Polarimetric Radar Observations: Methods and Examples. *Atmos. Meas. Tech.* **2022**, *15*, 1033–1054. [CrossRef]
4. Morrison, H.; van Lier-Walqui, M.; Fridlind, A.M.; Grabowski, W.W.; Harrington, J.Y.; Hoose, C.; Korolev, A.; Kumjian, M.R.; Milbrandt, J.A.; Pawlowska, H.; et al. Confronting the Challenge of Modeling Cloud and Precipitation Microphysics. *J. Adv. Model. Earth Syst.* **2020**, *12*, e2019MS001689. [CrossRef]
5. Morrison, H.; Tessendorf, S.A.; Ikeda, K.; Thompson, G. Sensitivity of a Simulated Midlatitude Squall Line to Parameterization of Raindrop Breakup. *Mon. Weather Rev.* **2012**, *140*, 2437–2460. [CrossRef]
6. Bao, J.-W.; Michelson, S.A.; Grell, E.D. Microphysical Process Comparison of Three Microphysics Parameterization Schemes in the WRF Model for an Idealized Squall-Line Case Study. *Mon. Weather Rev.* **2019**, *147*, 3093–3120. [CrossRef]
7. Li, H.; Huang, Y.; Luo, Y.; Xiao, H.; Xue, M.; Liu, X.; Feng, L. Does "Right" Simulated Extreme Rainfall Result from the "Right" Representation of Rain Microphysics? *Q. J. R. Meteorol. Soc.* **2023**, *149*, 3220–3249. [CrossRef]
8. Morrison, H.; Milbrandt, J.A. Parameterization of Cloud Microphysics Based on the Prediction of Bulk Ice Particle Properties. Part I: Scheme Description and Idealized Tests. *J. Atmos. Sci.* **2015**, *72*, 287–311. [CrossRef]
9. Johnson, M.; Jung, Y.; Dawson, D.T.; Xue, M. Comparison of Simulated Polarimetric Signatures in Idealized Supercell Storms Using Two-Moment Bulk Microphysics Schemes in WRF. *Mon. Weather Rev.* **2016**, *144*, 971–996. [CrossRef]
10. Kessler, E. On the Distribution and Continuity of Water Substance in Atmospheric Circulations. In *On the Distribution and Continuity of Water Substance in Atmospheric Circulations*; Kessler, E., Ed.; Meteorological Monographs; American Meteorological Society: Boston, MA, USA, 1969; pp. 1–84. ISBN 978-1-935704-36-2.
11. Morrison, H.; Curry, J.A.; Khvorostyanov, V.I. A New Double-Moment Microphysics Parameterization for Application in Cloud and Climate Models. Part I: Description. *J. Atmos. Sci.* **2005**, *62*, 1665–1677. [CrossRef]
12. Morrison, H.; Thompson, G.; Tatarskii, V. Impact of Cloud Microphysics on the Development of Trailing Stratiform Precipitation in a Simulated Squall Line: Comparison of One- and Two-Moment Schemes. *Mon. Weather Rev.* **2009**, *137*, 991–1007. [CrossRef]
13. Dawson, D.T.; Xue, M.; Milbrandt, J.A.; Yau, M.K. Comparison of Evaporation and Cold Pool Development between Single-Moment and Multimoment Bulk Microphysics Schemes in Idealized Simulations of Tornadic Thunderstorms. *Mon. Weather Rev.* **2010**, *138*, 1152–1171. [CrossRef]

14. Jung, Y.; Xue, M.; Zhang, G. Simulations of Polarimetric Radar Signatures of a Supercell Storm Using a Two-Moment Bulk Microphysics Scheme. *J. Appl. Meteorol. Climatol.* **2010**, *49*, 146–163. [CrossRef]

15. Putnam, B.J.; Xue, M.; Jung, Y.; Snook, N.; Zhang, G. The Analysis and Prediction of Microphysical States and Polarimetric Radar Variables in a Mesoscale Convective System Using Double-Moment Microphysics, Multinetwork Radar Data, and the Ensemble Kalman Filter. *Mon. Weather Rev.* **2014**, *142*, 141–162. [CrossRef]

16. Rutledge, S.A.; Hobbs, P. The Mesoscale and Microscale Structure and Organization of Clouds and Precipitation in Midlatitude Cyclones. VIII: A Model for the "Seeder-Feeder" Process in Warm-Frontal Rainbands. *J. Atmos. Sci.* **1983**, *40*, 1185–1206. [CrossRef]

17. Rutledge, S.A.; Hobbs, P.V. The Mesoscale and Microscale Structure and Organization of Clouds and Precipitation in Midlatitude Cyclones. XII: A Diagnostic Modeling Study of Precipitation Development in Narrow Cold-Frontal Rainbands. *J. Atmos. Sci.* **1984**, *41*, 2949–2972. [CrossRef]

18. Hong, S.-Y.; Lim, J. The WRF Single-Moment 6-Class Microphysics Scheme (WSM6). *Asia-Pac. J. Atmos. Sci.* **2006**, *42*, 129–151.

19. Lim, K.-S.S.; Hong, S.-Y. Development of an Effective Double-Moment Cloud Microphysics Scheme with Prognostic Cloud Condensation Nuclei (CCN) for Weather and Climate Models. *Mon. Weather Rev.* **2010**, *138*, 1587–1612. [CrossRef]

20. Gilmore, M.S.; Straka, J.M.; Rasmussen, E.N. Precipitation Uncertainty Due to Variations in Precipitation Particle Parameters within a Simple Microphysics Scheme. *Mon. Weather Rev.* **2004**, *132*, 2610–2627. [CrossRef]

21. Morrison, H.; Milbrandt, J. Comparison of Two-Moment Bulk Microphysics Schemes in Idealized Supercell Thunderstorm Simulations. *Mon. Weather Rev.* **2011**, *139*, 1103–1130. [CrossRef]

22. Bryan, G.H.; Morrison, H. Sensitivity of a Simulated Squall Line to Horizontal Resolution and Parameterization of Microphysics. *Mon. Weather Rev.* **2012**, *140*, 202–225. [CrossRef]

23. Adams-Selin, R.D.; van den Heever, S.C.; Johnson, R.H. Impact of Graupel Parameterization Schemes on Idealized Bow Echo Simulations. *Mon. Weather Rev.* **2013**, *141*, 1241–1262. [CrossRef]

24. Reinhardt, T.; Seifert, A. A Three-Category Ice Scheme for LMK. *Cosmo Newsl.* **2006**, *6*, 115–120.

25. Weverberg, K.V.; Vogelmann, A.M.; Lin, W.; Luke, E.P.; Cialella, A.; Minnis, P.; Khaiyer, M.; Boer, E.R.; Jensen, M.P. The Role of Cloud Microphysics Parameterization in the Simulation of Mesoscale Convective System Clouds and Precipitation in the Tropical Western Pacific. *J. Atmos. Sci.* **2013**, *70*, 1104–1128. [CrossRef]

26. Weverberg, K.V.; Vogelmann, A.M.; Morrison, H.; Milbrandt, J.A. Sensitivity of Idealized Squall-Line Simulations to the Level of Complexity Used in Two-Moment Bulk Microphysics Schemes. *Mon. Weather Rev.* **2012**, *140*, 1883–1907. [CrossRef]

27. Baumgardner, D.; Brenguier, J.L.; Bucholtz, A.; Coe, H.; DeMott, P.; Garrett, T.J.; Gayet, J.F.; Hermann, M.; Heymsfield, A.; Korolev, A.; et al. Airborne Instruments to Measure Atmospheric Aerosol Particles, Clouds and Radiation: A Cook's Tour of Mature and Emerging Technology. *Atmos. Res.* **2011**, *102*, 10–29. [CrossRef]

28. Ryzhkov, A.V.; Zrnic, D.S. *Radar Polarimetry for Weather Observations*; Springer Atmospheric Sciences; Springer International Publishing: Cham, Switzerland, 2019; ISBN 978-3-030-05092-4.

29. Ryzhkov, A.; Pinsky, M.; Pokrovsky, A.; Khain, A. Polarimetric Radar Observation Operator for a Cloud Model with Spectral Microphysics. *J. Appl. Meteorol. Climatol.* **2011**, *50*, 873–894. [CrossRef]

30. Snyder, J.C.; Bluestein, H.B.; Ii, D.T.D.; Jung, Y. Simulations of Polarimetric, X-Band Radar Signatures in Supercells. Part I: Description of Experiment and Simulated Phv Rings. *J. Appl. Meteorol. Climatol.* **2017**, *56*, 1977–1999. [CrossRef]

31. Zhou, A.; Zhao, K.; Lee, W.-C.; Ding, Z.; Lu, Y.; Huang, H. Evaluation and Modification of Microphysics Schemes on the Cold Pool Evolution for a Simulated Bow Echo in Southeast China. *J. Geophys. Res. Atmos.* **2022**, *127*, e2021JD035262. [CrossRef]

32. Jung, Y.; Zhang, G.; Xue, M. Assimilation of Simulated Polarimetric Radar Data for a Convective Storm Using the Ensemble Kalman Filter. Part I: Observation Operators for Reflectivity and Polarimetric Variables. *Mon. Weather Rev.* **2008**, *136*, 2228–2245. [CrossRef]

33. Wang, H.; Kong, F.; Jung, Y.; Wu, N.; Yin, J. Quality Control of S-Band Polarimetric Radar Measurements for Data Assimilation. *J. Appl. Meteorol. Sci.* **2018**, *29*, 546.

34. Yang, K.; He, J.; Tang, W.; Lu, H.; Qin, J.; Chen, Y.; Li, X. *China Meteorological Forcing Dataset (1979–2018)*; National Tibetan Plateau: Beijing, China, 2019.

35. Dawson, D.T.; Mansell, E.R.; Jung, Y.; Wicker, L.J.; Kumjian, M.R.; Xue, M. Low-Level ZDR Signatures in Supercell Forward Flanks: The Role of Size Sorting and Melting of Hail. *J. Atmos. Sci.* **2014**, *71*, 276–299. [CrossRef]

36. *GB/T 28592-2012*; The Grade of Precipitation. China Standards Press: Beijing, China, 2012.

37. Taylor, K.E. Summarizing Multiple Aspects of Model Performance in a Single Diagram. *J. Geophys. Res. Atmos.* **2001**, *106*, 7183–7192. [CrossRef]

38. Qian, Q.; Lin, Y.; Luo, Y.; Zhao, X.; Zhao, Z.; Luo, Y.; Liu, X. Sensitivity of a Simulated Squall Line During Southern China Monsoon Rainfall Experiment to Parameterization of Microphysics. *J. Geophys. Res. Atmos.* **2018**, *123*, 4197–4220. [CrossRef]

39. Wu, D.; Zhang, F.; Chen, X.; Ryzhkov, A.; Zhao, K.; Kumjian, M.R.; Chen, X.; Chan, P.-W. Evaluation of Microphysics Schemes in Tropical Cyclones Using Polarimetric Radar Observations: Convective Precipitation in an Outer Rainband. *Mon. Weather Rev.* **2021**, *149*, 1055–1068. [CrossRef]

40. Putnam, B.J.; Xue, M.; Jung, Y.; Zhang, G.; Kong, F. Simulation of Polarimetric Radar Variables from 2013 CAPS Spring Experiment Storm-Scale Ensemble Forecasts and Evaluation of Microphysics Schemes. *Mon. Weather Rev.* **2017**, *145*, 49–73. [CrossRef]

41. Wang, M.; Zhao, K.; Pan, Y.; Xue, M. Evaluation of Simulated Drop Size Distributions and Microphysical Processes Using Polarimetric Radar Observations for Landfalling Typhoon Matmo (2014). *J. Geophys. Res. Atmos.* **2020**, *125*, e2019JD031527. [CrossRef]

42. Chen, J.-P.; Tsai, T.-C. Triple-Moment Modal Parameterization for the Adaptive Growth Habit of Pristine Ice Crystals. *J. Atmos. Sci.* **2016**, *73*, 2105–2122. [CrossRef]
43. Mallick, C.; Dutta, U.; Bhowmik, M.; Mohan, G.M.; Hazra, A.; Ghosh, R.; Pawar, S.D.; Chen, J.-P. Comparison of Two-Moment and Three-Moment Bulk Microphysics Schemes in Thunderstorm Simulations over Indian Subcontinent. *Atmos. Res.* **2024**, *310*, 107614. [CrossRef]
44. Hong, S.-Y.; Dudhia, J.; Chen, S.-H. A Revised Approach to Ice Microphysical Processes for the Bulk Parameterization of Clouds and Precipitation. *Mon. Weather Rev.* **2004**, *132*, 103–120. [CrossRef]
45. Houze, R.A.; Hobbs, P.V.; Herzegh, P.H.; Parsons, D.B. Size Distributions of Precipitation Particles in Frontal Clouds. *J. Atmos. Sci.* **1979**, *36*, 156–162. [CrossRef]